International Journal of Rock Mechanics & Mining Sciences 186 (2025) 106024

Contents lists available at ScienceDirect

International Journal of Rock Mechanics and Mining Sciences

journal homepage: www.elsevier.com/locate/ijrmms

Elastic wave propagation and attenuation across cemented rock fractures under tension

Hui Yang [a], Qi Zhao [a,*], Dongya Han [b,**], Qinghua Lei [c,d], Huanyu Wu [a], Xiaolin Huang [e], Zhiyi Chen [f], Yu Huang [f]

[a] Department of Civil and Environmental Engineering, The Hong Kong Polytechnic University, China
[b] School of Resources and Safety Engineering, Central South University, 410083, Changsha, Hunan, China
[c] Department of Earth Sciences, ETH Zurich, Zurich, Switzerland
[d] Department of Earth Sciences, Uppsala University, Uppsala, Sweden
[e] Department of Civil Engineering, School of Human Settlements and Civil Engineering, Xi'an Jiaotong University, 710049, Xi'an, Shaanxi, China
[f] Department of Geotechnical Engineering, College of Civil Engineering, Tongji University, 200092, Shanghai, China

ARTICLE INFO

Keywords:
Elastic wave propagation
Cemented rock fractures
Tensile stress
Fracture stiffness
Microstructures

ABSTRACT

Tensile loading plays a critical role in geological processes like landslides and earthquakes, as well as engineering applications such as hydraulic fracturing and tunnel excavation. We investigate elastic wave behavior across cemented rock fractures under tensile stress conditions. Ultrasonic measurements and uniaxial direct tension tests were performed concurrently on quartz diorite and diabase specimens with and without individual cemented fractures to determine the influence of tensile stress on the characteristics of elastic waves. Results show that increasing tensile stress leads to enhanced wave attenuation and reduced velocity, amplitudes, and dominant frequency of transmitted waves. These changes are primarily driven by the formation and growth of microcracks near cemented rock fractures under tensile stress. The jointed quartz diorite samples experienced progressive reductions in static and dynamic fracture stiffness. In contrast, jointed diabase samples maintained nearly constant static fracture stiffness and only saw decreases in dynamic fracture stiffness. The reduction in dynamic fracture stiffness is attributed to microscopic damage that modifies elastic wave velocity and dissipation but is not captured by static stress-strain measurements. The gradual decrease in dynamic fracture stiffness reflects stable crack growth, while sudden reductions indicate crack coalescence at the interface. We propose that dynamic fracture stiffness, assessable with seismic wave measurement, is a more reliable indicator of tensile damage than static fracture stiffness due to its sensitivity to low strains and ability to capture microstructural changes. These findings provide valuable insights into seismic methods applied to assess stress conditions on rock discontinuities in the field.

1. Introduction

Rock fractures are ubiquitous in the Earth's crust and play an important role in physical and chemical processes that are relevant to tectonic activities (e.g., earthquake rupture and volcanic eruption) and engineering applications (e.g., hydrocarbon recovery, CO_2 sequestration, nuclear waste storage, underground excavation, and geothermal energy extraction). Stress states on rock fractures commonly change with natural events, such as fault slip and deep tectonic tremor, and anthropogenic activities, such as hydraulic fracturing and underground excavation. The change in stress state influences the properties of rock fractures and then affects wave propagation and attenuation in subsurface rock masses.[1–4] However, stress conditions in underground rock mass are challenging to access due to limited direct access for observation and measurement. Geophysical surveys using elastic waves have proved to be among the most promising tools in capturing the stress-dependent behavior of rocks and assessing the state of stress along rock fractures.[5–9] Therefore, the stress dependence of elastic wave properties across rock fractures has attracted considerable attention from geoengineering and geophysics communities.

* Corresponding author.
** Corresponding author.
E-mail addresses: qi.qz.zhao@polyu.edu.hk (Q. Zhao), dongyahan@csu.edu.cn (D. Han).

https://doi.org/10.1016/j.ijrmms.2025.106024
Received 7 March 2024; Received in revised form 6 November 2024; Accepted 5 January 2025
Available online 7 January 2025

In the laboratory, the stress dependence of elastic wave propagation across rock fractures has been extensively studied through the combination of ultrasonic monitoring and mechanical loading tests.[4,10–18] Past experimental studies revealed that, for normal incidence of P and S waves upon single non-weld rock fractures under uniaxial compression, increasing compressive stress led to (i) an increase in the wave velocity, (ii) an increase in the transmitted energy, (iii) an increase in the amplitude of the spectral peak, and (iv) a shift of spectral peak toward the higher frequency.[10,13,14] For P and S waves propagation across a rock fracture under the mixed compressive and shear stress state, increasing shear stress resulted in higher wave velocity and amplitude during the elastic loading period with near-zero local slip rate.[11,15,16,18] After reaching the peak shear stress, wave velocity and amplitude decreased with the reduction in shear stress and an abrupt increase in the local slip rate.[11,15,16,18] Observations by Nakagawa et al.[19] showed that the shear stress applied to a rock fracture caused partial conversion between P- and S-waves. The increasing shear stress enhanced the amplitude of the shear-induced converted waves but moderately affected directly transmitted waves across the rock fracture.[19] Recent studies have documented acoustic measurements on individual rock fractures under uniaxial normal stress and pore pressure oscillations.[20–22] It was found that elastic wave velocity and spectral amplitude oscillate following the same trend as the pore pressure oscillations. Additionally, the imposed shear loading moderately reduced the relative change in wave velocity caused by the dynamic stress. Recent work on multifrequency ultrasonic approach and wave transmission across nonlinear rock joints has provided new insights into extracting static modulus and understanding damage characteristics in complex rock masses under compression.[23,24]

However, the majority of past studies have focused on compressive and shear stress conditions, with relatively little attention given to tensile stress effects on wave propagation across rock fractures. This is due to the conventional viewpoint that rock fractures are open or weakly connected and incapable of supporting tensile loading. Contrary to this perspective, field surveys and laboratory studies have demonstrated that certain rock fractures (e.g., veins, dikes) are cemented with diagenetic materials,[25–27] allowing them to withstand tensile stresses up to several megapascals.[28–30] In many natural and anthropogenic events, such as the formation of basins in buried sediments,[31] fault sliding and earthquake rupturing,[32] and the stress redistribution caused by tunneling and mining operations,[33] rock fractures could locally endure tensile loading. Thus, the knowledge concerning elastic wave propagation across cemented rock fractures under tension is of great practical and scientific significance for many geophysical and geotechnical disciplines. To address this gap, we developed an experimental approach combining ultrasonic pulse transmission and direct tensile testing to examine wave propagation across rock fractures under tensile stress. Our preliminary work investigated the tension dependency of elastic wave behaviors in natural limestone veins.[34] Nevertheless, the limited data from limestone specimens were insufficient to generalize the tension-dependent wave behaviors observed across cemented rock fractures.

In this study, laboratory experiments are carried out on artificially cemented fractures to advance our understanding of the elastic wave behavior across cemented rock fractures subjected to tensile loading. We adopt the quartz diorite and diabase as the host rock of synthetic cemented fractures to investigate the effects of the host rock type. The experimental results show that the wave velocity, amplitudes, and dominant frequency decrease while wave attenuation increases upon the increased tensile load. The relative changes in elastic wave properties for rock samples with single cemented fractures could be larger or smaller than those for their intact counterparts, depending on the host rock lithology. We perform the thin-section analysis of post-mortem cemented rock fractures to understand the tension-induced evolution of elastic wave attributes regarding microstructural features and cracking patterns of rock specimens. The quartz diorite has greater heterogeneities in grains and micro defects than the diabase, causing a more complex cracking mode and more significant changes in wave properties for jointed quartz diorite specimens. The dynamic and static fracture stiffness are estimated using the inverse hyperbolic and displacement discontinuity models to analyze the bulk behavior of cemented rock fractures under tension. Both dynamic and static fracture stiffness for jointed quartz diorite continuously decrease with the increasing tensile load. By contrast, the dynamic fracture stiffness gradually declines while the static fracture stiffness remains almost constant for jointed diabase specimens under tension.

2. Materials and methods

2.1. Specimen preparation

This study adopted a quartz diorite from Fujian Province, China, and a diabase from Inner Mongolia, China, as host rocks for preparing synthetic cemented fractures, with an ultra-high-performance cement developed by Teng et al.[35] as the filling material to artificially cement the fractures. The quartz diorite consists of 75 % plagioclase, 10 % quartz, 7 % biotite, 6 % hornblende, and less than 2 % of augite, apatite, and zircon; its lath-shaped plagioclase grains have a size between 0.1 mm–0.2 mm for the short axis and 0.6 mm–1.5 mm for the long axis (Fig. 1a). The diabase has a mineralogical composition of 55 % plagioclase, 44 % augite, and less than 1 % of olivine and zircon; the dimensions of lath-shaped plagioclase grains are 0.15–0.3 mm and 0.6–1.0 mm for the short and long axes, respectively (Fig. 1a). The ultra-high-performance cement comprises Portland cement (57.7 % wt.), silica fume (14.4 % wt.), quartz powder (14.4 % wt.), high-range water reducer (2.1 % wt.), and water (11.4 % wt.).[35] This cement has a higher tensile strength than the host rocks, thus allowing us to investigate the influences of host rock and cement-rock bonding on the properties of elastic waves propagating across the fractures subjected to tensile loading.

Four rock cylinders with 49 mm in diameter and 100 mm in length were first prepared using each host rock (quartz diorite or diabase). Then, a through-going fracture was introduced in the middle of three rock cylinders via a modified Brazilian test[36] (Fig. 1c). The fracture surfaces were characterized using a three-dimensional scanner (Carl Zeiss Comet L3D 5M). After that, the ultra-high-performance cement with a mass of 10 g was sandwiched between two halves of a rock cylinder to create a cemented rock fracture. Following the same process, six fractured rock specimens, i.e., QD-F-1, QD-F-2, and QD-F-3, with the quartz diorite as host rock and D-F-1, D-F-2, and D-F-3 with the diabase as host rock, were produced for this study (Fig. 1b). The remaining two intact rock cylinders, labeled by QD-I and D-I, were used to ascertain reference measurements (Fig. 1b). Note that the end surfaces of all rock specimens were polished to ensure flatness and parallelism. In addition, an intact aluminum specimen with identical dimensions to rock specimens was prepared to calibrate the experimental test system. The aluminum specimen was also used as the reference to evaluate wave attenuation in rock samples. The mechanical and physical properties of all materials used in this study are given in Table 1.

2.2. Experimental setup and procedure

This study employed a test configuration that integrated an ultrasonic testing system with a displacement-controlled loading system to perform simultaneous ultrasonic pulse-transmission measurements and uniaxial tension tests on rock specimens (Fig. 2a). The ultrasonic testing system[38] consists of an Olympus pulser/receiver (model 5077 PR), a pair of Olympus P-wave transducers at a frequency of 1 MHz (model V192), a Tektronix digital oscilloscope (DPO 2012B), and a computer for data acquisition laptop, was applied to take acoustic measurements in this study. The two P-wave transducers, connected to the pulser/receiver, were aligned and positioned at the ends of the rock sample for pulse transmission testing.[38–40] During each measurement, one transducer converted the square signal from the pulser/receiver into an incident

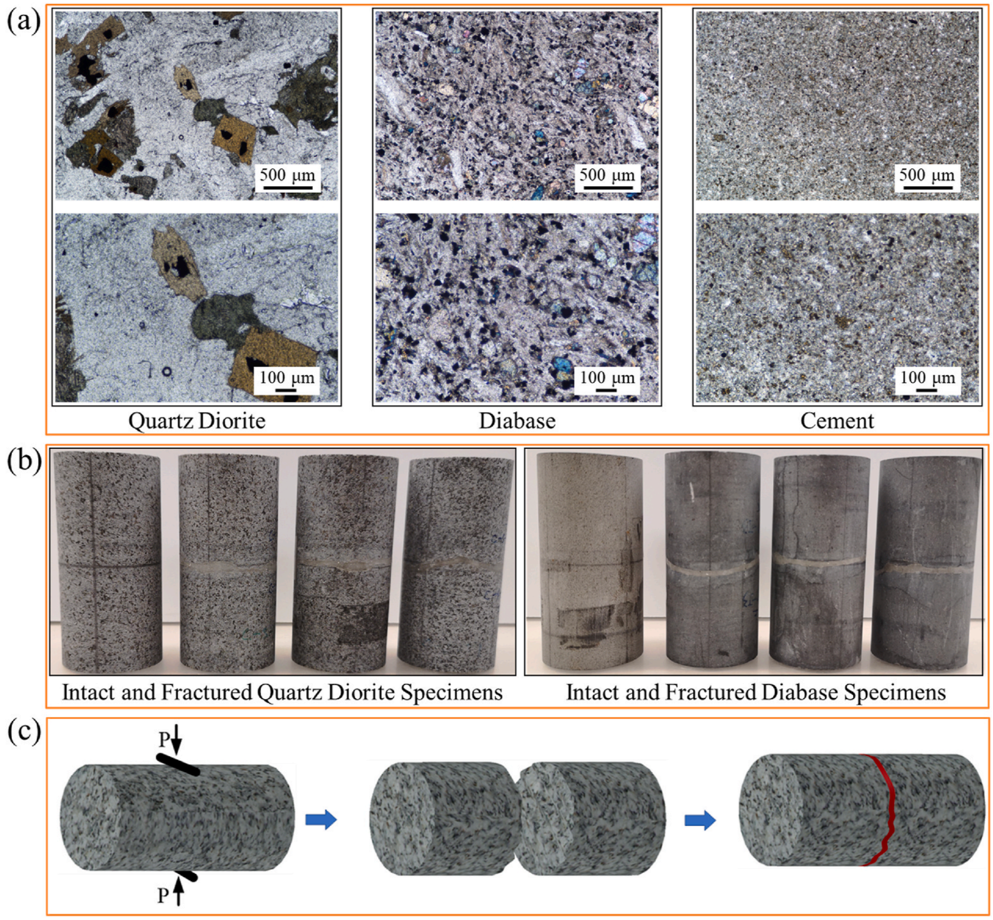

Fig. 1. Rock specimens used in this study: (a) Micrographic images of thin sections of quartz diorite (left), diabase (center), and cement (right), (b) Photographs of intact and fractured quartz diorite (left) and diabase (right) specimens, and (c) illustration of modified Brazilian test.

Table 1
Basic Physical and Mechanical Properties of Materials Used in this Study.

Materials	Uniaxial compressive strength [MPa]	Uniaxial tensile strength [MPa]	Young's modulus [GPa]	Bulk density [kg/m^3]	Poisson's ratio	Porosity [%]
Quartz Diorite	215.2	5.2	74.90	2807	0.33	0.54
Diabase	360.5	7.9	98.20	2915	0.35	0.42
Ultra-High-Performance Cement	193.8	8.6	46.76	2320	0.24	0.45
Aluminum	–	–	68.00[37]	2700[37]	0.33[37]	–

wave, which was introduced into the rock specimen. The other transducer detected the transmitted wave after it passed through the specimen. The transmitted signal was then digitized, displayed, and recorded by a digital oscilloscope. A custom-made connecting device was used to mount the ultrasonic transducers and the rock specimen onto the displacement-controlled loading test system.[34] Vaseline was applied between the specimen and the transducer interfaces before testing to ensure good coupling. The rock specimen was bonded to a metal cap using 3M DP460-NS epoxy resin, which was allowed to cure for 24 h to achieve sufficient bonding strength between the rock and the metal cap (Fig. 2b). Screws were then used to assemble the metal caps, ensuring the stability of the sample during tensile loading.

Before testing on rock specimens, a baseline test was conducted on the aluminum sample to calibrate the above-described test configuration. In the calibration test, the uniaxial tensile loading was applied to the aluminum sample at a constant strain rate of 1×10^{-5} s^{-1} until reaching 20 kN. Meanwhile, ultrasonic pulse-transmission tests were performed on the aluminum sample at every 1 kN increment. The transmitted waves collected from an aluminum sample under tension showed minimal changes at each loading step, consistent with theoretical expectations, confirming the stability and reliability of our experimental setup.[41,42] After the calibration, the test configuration was adopted to carry out experiments on rock specimens following the same procedure until their failure. The transmitted waveforms with a 100-μs duration were recorded at each increment of 1 kN during the tensile loading process. Note that 32 waveforms were stacked for each ultrasonic measurement to obtain a high signal-to-noise ratio. In addition, two 20 mm-long strain gauges were oppositely mounted on the middle of the surface of the tested rock sample to record the longitudinal strain.

2.3. Ultrasonic wave data processing

To quantitatively describe the behavior of elastic waves propagating across rock specimens, we compute a set of essential wave properties, including the P-wave velocity (V_P), peak-to-peak amplitude (A_{PTP}), maximum spectral amplitude (S_{max}), dominant frequency (f_d), and wave

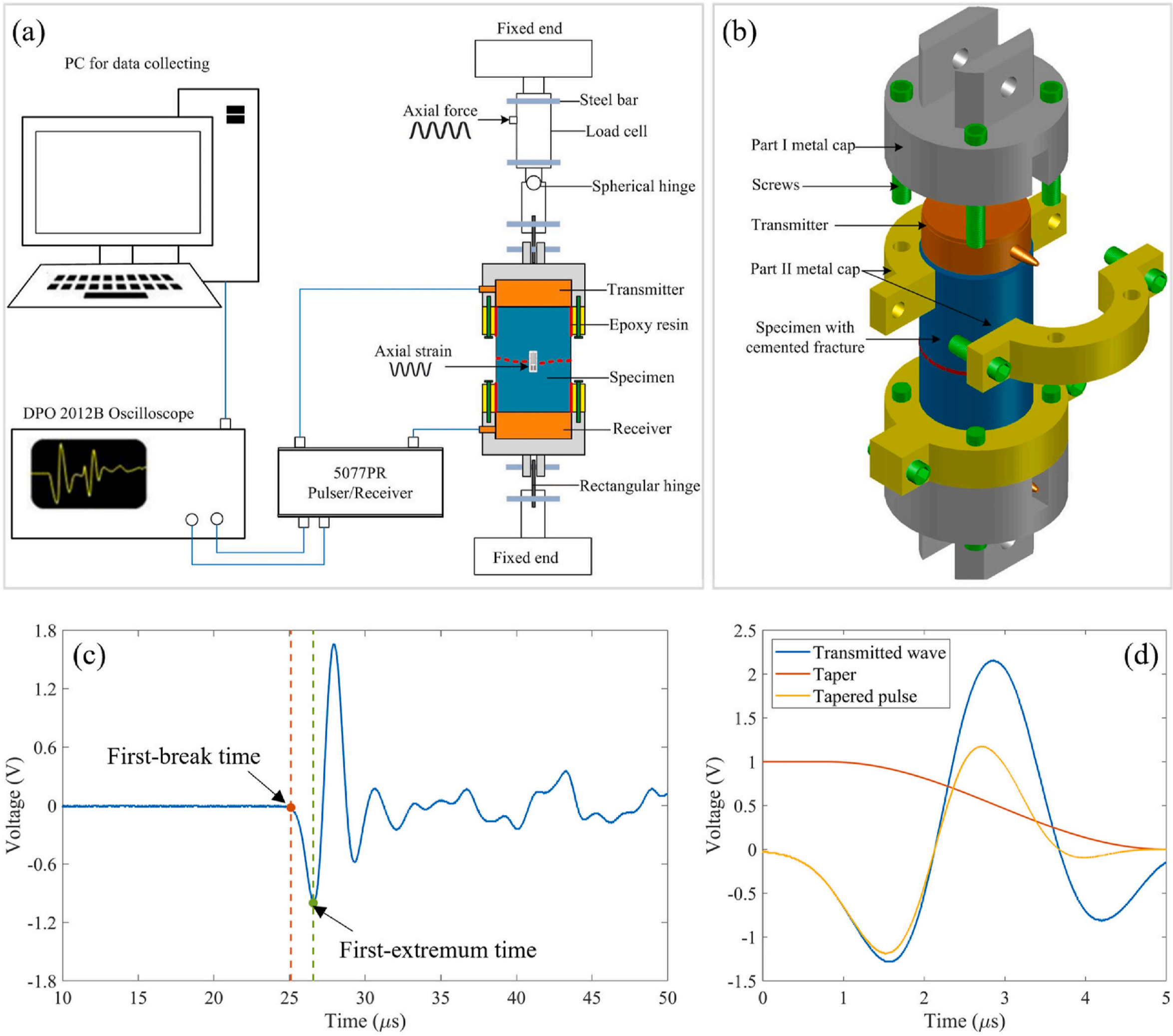

Fig. 2. Experimental setup and representative data for this study: (a) Schematic of the self-developed test configuration, (b) Illustration of the specimen-transducers assembly achieved by the custom-made connecting device, (c) Illustration of travel time picking using different methods, (d) Illustration of the extraction of first arriving pulses via a taper.

attenuation (1000/Q) from collected ultrasonic waveforms.

The P-wave velocity was computed as the sample length (L) divided by the travel time of transmitted waves (t), i.e., $V_P = L/t$. We determined the travel time by picking the first extremum and zero-crossing of pulse amplitude for calculating the first-extremum and first-break wave velocities, respectively (Fig. 2c). The first-extremum wave velocity (V_e) is determined by the first-extremum time at which the amplitude reaches its first extremum.[43] The travel time of pulses in rock specimens is corrected by measuring the difference in the timing of the first-extremum amplitude when the rock core lies between the transducers relative to when the transducers are placed directly in contact.[44] The first-break wave velocity (V_b) is calculated from the first-break time (i.e., onset time) at which the signal's energy is first detectable.[45] The onset time is less influenced by the dispersion-dependent waveform modification, which is more consistent than the first-extremum time relying on picking some later waveform features likely to be affected by wave dispersion.[44] Comparisons of wave velocities calculated from various methods are made in Table 2. Both first-extremum and first-break wave velocities exhibit similar trends with increasing tensile load.

In our experiment, the ultrasonic waveforms were less noise-contaminated and recorded at a high sampling rate (10^9 Hz) such that the Nyquist frequency (5×10^8 Hz) is much larger relative to their frequency bandwidth (10^5–10^6 Hz). Such high-fidelity signals allow greater accuracy in determining the onset time of signals[46]; thus, this study focuses only on the evolution of the first-break wave velocity.

The peak-to-peak amplitude, defined as the difference between the trough and peak amplitudes of the first-arriving pulse, was directly determined from the received waveforms. As illustrated in Fig. 2d, we extracted signals from the original waveforms through a taper function. Then we conducted the fast Fourier transform on the tapered signals to derive the frequency spectra,[10] with the maximum spectral amplitude and dominant frequency further determined. Based on the frequency spectra, the inverse of the quality factor (1/Q) was assessed through the spectral ratio method in which $\ln(A_1/A_2) = -\pi f L[(1/Q_1 v_1) - (1/Q_2 v_2)]$ (subscripts 1 and 2 denote the aluminum reference and the rock specimen, respectively) to quantify wave attenuation in rock specimens.[47]

Furthermore, we define the relative variation ($\Delta\Psi$) of an elastic wave property as a function of the normalized load using the ratio $\Delta\Psi = (\Psi_\tau - \Psi_0)/\Psi_0$, where Ψ_τ and Ψ_0 are values of the aforementioned elastic wave properties measured at a specific tensile load (Ψ_τ) and before tensile loading (Ψ_0), respectively.

2.4. Microstructural analysis

The tension-driven failed rock specimens were carefully reconstructed using transparent epoxy resin to prepare thin sections for petrographic microstructural analysis. The thin sections parallel to the

Table 2
Comparison of wave velocities calculated from different travel time-picking methods.

QD-I		QD-F-1		QD-F-2		QD-F-3		D-I		D-F-1		D-F-2		D-F-3		Force
V_e (m/s)	V_b (m/s)	V_e (m/s)	V_b (m/s)	V_e (m/s)	V_b (m/s)	V_e (m/s)	V_b (m/s)	V_e (m/s)	V_b (m/s)	V_e (m/s)	V_b (m/s)	V_e (m/s)	V_b (m/s)	V_e (m/s)	V_b (m/s)	F_τ (kN)
4168.68	4228.23	4002.93	4103.05	4107.70	4210.77	4074.31	4211.71	6240.93	6145.22	6196.75	6068.52	6032.43	5927.68	6180.61	6075.84	0
4157.87	4222.66	3985.82	4086.73	4096.67	4204.05	7061.60	4207.34	6240.93	6144.66	6196.19	6067.98	6032.07	5927.16	6180.23	6075.48	1
4151.88	4213.80	3961.49	4059.93	4077.00	4183.85	4043.24	4193.53	6240.74	6143.90	6196.00	6067.80	6031.53	5925.77	6179.10	6074.20	2
4132.21	4194.43	3934.53	4033.88	4048.69	4160.60	4020.51	4169.85	6238.39	6142.20	6195.06	60.66.89	6031.35	5924.91	6178.35	6073.11	3
4114.86	4177.08	3899.97	4003.16	4020.53	4131.37	3993.00	4147.28	6236.06	6141.25	6194.68	6066.17	6030.81	5924.04	6177.97	6072.56	4
4094.28	4159.35	3867.04	3971.12	3989.07	4099.65	3964.47	4121.61	6233.52	6139.55	6193.93	6065.99	6030.09	5922.49	6176.84	6071.47	5
4076.74	4141.08	3834.87	3937.75	3956.32	4063.69	3939.17	4086.45	6230.99	6138.80	6193.55	6065.63	6029.56	5921.79	6176.08	6070.20	6
4054.30	4121.25	3798.60	3902.15	3923.96	4030.43	3906.44	4060.63	6227.49	6138.04	6192.04	6065.27	6028.48	5920.93	6174.77	6069.29	7
4033.83	4100.44	3764.90	3864.45	3887.79	3993.07	3875.72	4023.30	6225.36	6136.72	6190.72	6062.38			6174.01	6068.56	8
4011.78	4074.98	3723.83	3828.20			3841.05	3988.14	6224.00	6133.70					6172.32	6066.56	9
3987.57	4042.11							6222.64	6131.82					6171.76	6062.20	10
								6221.09	6130.31					6169.12	6056.58	11
								6219.15	6127.11							12
								6216.44	6122.97							13
								6213.53	6120.16							14

Note. F_τ is the tensile load.

loading direction were cut from the epoxied post-mortem cemented rock fractures. The Nikon Eclipse 50i POL Polarizing Microscope equipped with a digital camera was employed to identify and capture the microstructural features of the well-prepared thin sections. We manually identified the microscopic scale defects, including microcracks and pores in the representative thin sections, and conducted quantitative analysis.

2.5. *Methods for estimating static and dynamic fracture stiffness*

The fracture stiffness is defined as the ratio of the incremental stress across the fracture to the corresponding incremental displacement. In the quasi-static mechanical case, the static fracture stiffness (κ_S) is represented by the slope of the tangent to the stress-displacement. The fracture deformation can be determined by subtracting the deformation of the host rock from the total deformation of a fractured rock sample.[48] For jointed rock specimens with the linear tensile stress-displacement relation, κ_S can be obtained from a linear fitting of the stress versus displacement curve; while for jointed rock specimens with a nonlinear deformational behavior under tension, κ_S can be calculated by fitting the tensile stress-displacement curves via the empirical model in the following[34]

$$\kappa_S = \frac{\frac{1}{\kappa_i}}{\left(\frac{1}{\kappa_i} + \frac{d}{\alpha\sigma_t}\right)^2} \tag{1}$$

where d is the displacement of the cemented fracture under tension, κ_i is the initial fracture stiffness at zero tensile stress, σ_t is the tensile strength of rock joints, and α is a correction factor.

On the other hand, dynamic fracture stiffness (κ_D) is related to the transient evolution of elastic waves accompanied by dynamic rock fracture deformation. Based on the displacement discontinuity model, the measured wave velocity and the spectral amplitudes can be used to calculate the transmission coefficient ($|T(\omega)|$) across a rock fracture as[10]

$$|T(\omega)| = \left[\frac{4\left(\frac{\kappa_D}{Z}\right)^2}{4\left(\frac{\kappa_D}{Z}\right)^2 + \omega^2}\right]^{\frac{1}{2}} \tag{2}$$

where ω is the angular frequency, κ_D is the dynamic fracture stiffness, and Z is the wave impedance given by the product of rock density and phase velocity. κ_D equals to the value that produces the best linear regression between the theoretically predicted and experimentally measured frequency spectra. Note that κ_D can be frequency dependent.[49]

3. Results

3.1. *Mechanical responses of rock specimens under tension*

Fig. 3a shows that the stress-strain curves of both intact and jointed quartz diorite specimens are nonlinear from the beginning of the loading to the failure (i.e., peak stress). The higher the degree of nonlinearity, the lower the uniaxial tensile strength (UTS), but the larger the failure strain (FS). Regardless of the existence of cemented fractures, the slope of stress-strain curves (i.e., effective modulus) of quartz diorite specimens gradually decreases with the increasing tensile stress (Fig. 3a). The quartz diorite specimens with cemented fractures have lower UTSs than the intact specimens. The average UTS of jointed quartz diorite specimens is 4.93 ± 0.35 MPa, i.e., about 90 % ± 6 % of the UTS of the intact quartz diorite sample. In addition, the jointed quartz diorite specimens exhibit larger FS than the intact counterpart. The mean FS of jointed quartz diorite specimens is 225 ± 47 με, which is around 134 % ± 28 % of that of the intact quartz diorite specimen.

In contrast, the stress-strain curves of all diabase specimens are nearly linear up to failure, exhibiting a typical brittle failure behavior for

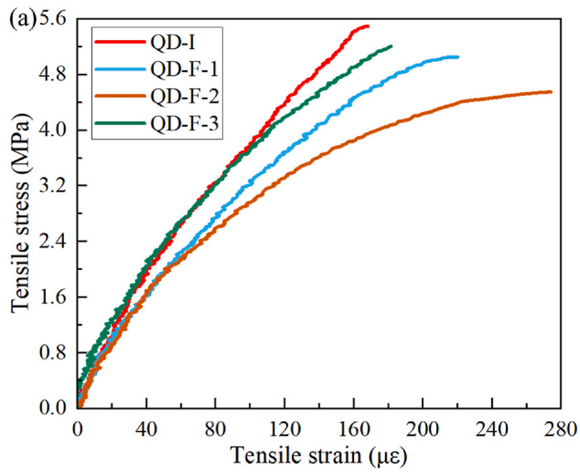

Fig. 3. The tensile stress-strain relationships for (a) Quartz diorite specimens and (b) Diabase specimens.

both intact and jointed diabase specimens (Fig. 3b). The effective modulus for diabase specimens with cemented fractures is lower than that for the intact diabase specimen. The jointed diabase specimens have lower UTSs compared to the intact sample. The UTS of diabase specimens with cemented fracture varies from 3.87 to 6.47 MPa, approximately 49 %–82 % of the intact diabase. The FS of jointed diabase specimens could be larger or smaller than that of the intact diabase sample. There is no clear correlation among the effective modulus, UTS, and FS for all diabase specimens. D-F-3 has UTS and FS similar to D-I, and D-F-1 has UTS and FS similar to D-F-2. It is likely due to localized microstructural variations at the cement interface or within the diabase matrix. These variations may result from heterogeneities in grain size, microcracks, and cement bonding quality, leading to differences in fracture behavior.

The comparison between Fig. 3a and b indicates that the UTS of the intact quartz diorite specimen is smaller than that of the intact diabase specimen. By contrast, jointed quartz diorite specimens have higher or lower UTS than jointed diabase specimens. In addition, the FS of quartz diorite specimens is much greater than that of the diabase specimens.

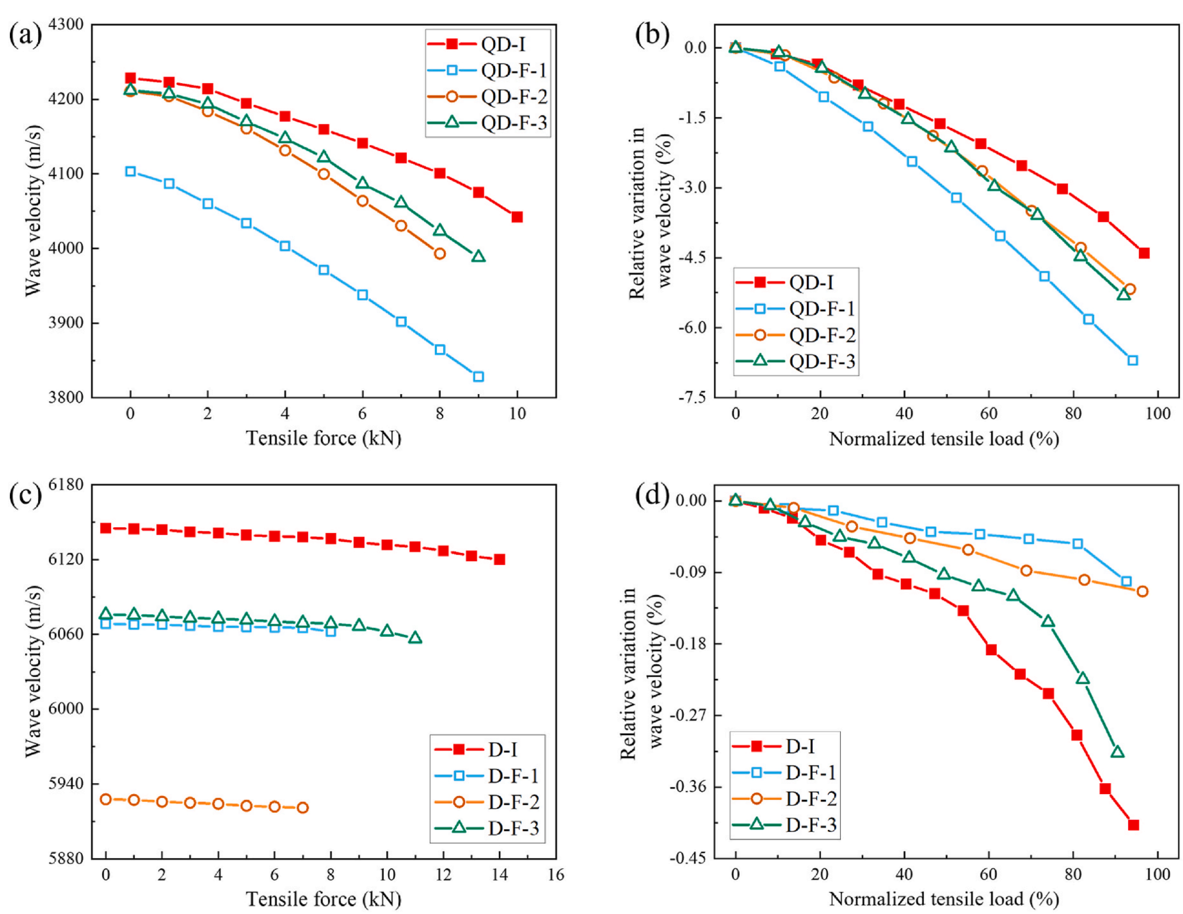

Fig. 4. Wave velocity and its relative variation during the tensile loading process for (a–b) Quartz diorite specimens and (c–d) Diabase specimens. The normalized tensile load is determined by normalizing a specific tensile load to the ultimate load at the tensile failure.

3.2. Elastic wave properties in rock specimens under tension

3.2.1. Wave velocity

Independent of the host rock type, the wave velocity (V_P) in intact and jointed rock specimens decreases with the increasing tensile load, where jointed rock specimens exhibit lower wave velocities than the intact ones (Fig. 4). V_P for quartz diorite specimens is in the range of 3800–4250 m/s, which is lower than that for diabase specimens in the range of 5900–6140 m/s (Fig. 4a & c). The relative reduction and decreasing rate in V_P for quartz diorite specimens are more significant than those for diabase specimens (Fig. 4b & d). V_P in quartz diorite specimens exhibits a maximum drop of 4 %–7 %, while the maximum reduction in V_P for diabase specimens ranges from 0.09 % to 0.42 %. The decreasing trend of V_P for jointed quartz diorite specimens resembles that for the intact quartz diorite specimen (Fig. 4b). Besides, jointed quartz diorite specimens show more significant V_P reduction than the intact counterpart under the same tensile loading level, especially at higher tensile forces. These observations are consistent with stress-strain relations of quartz diorite specimens, where quartz diorite specimens with or without fractures exhibit a similar nonlinear deformational behavior, and jointed quartz diorite specimens have smaller UTSs and greater FS than the intact sample. By comparison, the relative decrease of V_P is smaller for jointed diabase specimens than for the intact diabase specimen at a given tensile load (Fig. 4d). Specifically, the V_P decreasing trend of D-F-3 is analogous to that of D-I, while D-F-1 and D-F-2 display a similar decreasing trend in V_P. This phenomenon corresponds to the stress-strain relations of diabase specimens, where D-F-3 has similar UTS and FS to D-I, and D-F-1 has comparable UTS and FS to D-F-2.

3.2.2. Wave amplitudes

The peak-to-peak amplitude (A_{PTP}) monotonically decreases as the tensile load increases for quartz diorite and diabase specimens (Fig. 5a & c). Independent of the host rock type, A_{PTP} for jointed rock samples is smaller than that for intact specimens at a given tensile load. The jointed quartz diorite specimens display a similar variation of A_{PTP} with the intact counterpart under tension (Fig. 5a). The A_{PTP} for jointed diabase specimens drops smoothly with the increasing tensile load, while it decreases at an increasing rate for the intact diabase specimen (Fig. 5c). A_{PTP} for quartz diorite specimens displays maximum decreases of 24 %–40 %, while the utmost reduction in A_{PTP} for diabase specimens is from 9 % to 45 % (Fig. 5b & d). The intact and jointed quartz diorite specimens exhibit similar A_{PTP} reduction trends with increasing tensile force (Fig. 5b). Under a specific tensile loading level, the relative A_{PTP} decrease for jointed quartz diorite specimens is comparable to that for the intact sample. By contrast, the jointed diabase specimens generally display a smaller A_{PTP} reduction than the intact diabase specimen, especially under high tensile forces (Fig. 5d). The relative A_{PTP} decrease for the intact diabase specimen increases at an increased rate throughout the tensile loading process. For tensile loads below 82 % of the ultimate load, D-F-1, D-F-2, and D-F-3 exhibit a similar APTP decreasing trend, with the APTP ultimately reducing by 7 %–8 %.

The maximum spectral amplitude (S_{max}) gradually decreases with the tensile force for quartz diorite and diabase specimens; the jointed rock specimens have smaller S_{max} than the intact samples (Fig. 5e & g). The tension-driven variation of S_{max} resembles that of the A_{PTP} decline. The S_{max} decrease is roughly identical to the A_{PTP} reduction for quartz diorite and diabase specimens at a specific tensile force (Fig. 5f & h). Specifically, the S_{max} reduction for QD-F-1 and QD-F-3 is more significant than that for QD-I, while QD-F-2 exhibits a similar trend of S_{max} drop compared to QD-I (Fig. 5f). The relative decrease in S_{max} for D-F-1, D-F-2, and D-F-3 is commonly smaller than that for D-I, particularly when the tensile load is high (Fig. 5h).

Compared to wave velocity (V_P), wave amplitudes (A_{PTP} and S_{max}) in quartz diorite and diabase specimens are less sensitive to tensile loading, except for the last data point. As the tensile load reaches approximately 90 % of the failure force, D-F-3 shows significant reductions in A_{PTP} and S_{max}. In contrast, A_{PTP} and S_{max} remain gently reduced for D-F-1 and D-F-2. This observation is consistent with wave velocity trends.

3.2.3. Dominant frequency

For both host rock types tested in this study, the dominant frequency (f_d) for intact and jointed rock specimens gradually shifts toward smaller values as the tensile load increases (Fig. 6). The values of f_d for quartz diorite specimens are at 0.24–0.37 MHz, lower than that for diabase specimens at 0.62–0.72 MHz (Fig. 6a & c). At a given tensile load, f_d for jointed quartz diorite specimens is smaller than that for the intact sample (Fig. 6a). In contrast, there is no clear correlation between the cemented fractures and f_d for diabase specimens (Fig. 6c). The values of f_d for D-F-1 and D-F-2 are lower than that for D-I, while D-F-2 exhibits a slightly larger f_d than D-I throughout the tension. The quartz diorite specimens display the maximum f_d drop of 9 %–22.5 %, while the dominant frequency for diabase specimens ultimately decreases by 2 %–7 % (Fig. 6b & d). The tension-driven f_d shifting tendency for jointed quartz diorite specimens is similar to that for the intact counterpart (Fig. 6b). The relative f_d decrease for QD-F-1 and QD-F-2 is close to that for QD-I, whereas QD-F-3 exhibits more significant f_d shifts than QD-I at a specific tensile loading level. By comparison, the tension-induced f_d drop for jointed diabase specimens is generally smaller than that for the intact diabase specimen, especially at the high-level tensile loading (Fig. 6d). D-F-1, D-F-2, and D-F-3 exhibit a similar f_d decreasing trend with a maximum f_d reduction of 2 %–2.5 %, whereas the f_d decrease for D-I accumulates at a faster rate to 7 % over the tensile process.

The evolution of dominant frequency (f_d) is in accord with that of wave velocity (V_P) and amplitudes (A_{PTP} and S_{max}) for rock specimens subjected to uniaxial tensile loading (Figs. 4–6). Compared to V_P, A_{PTP}, and S_{max}, the dominant frequency f_d displays local plateaus upon the rising tensile load. The f_d drop is generally greater than the V_P reduction but smaller than the decreases of A_{PTP} and S_{max} throughout the tensile loading.

3.2.4. Wave attenuation

Wave attenuation ($1000/Q$) in intact and jointed quartz diorite and diabase specimens linearly increases with the tension (Fig. 7a & c). The jointed quartz diorite specimens exhibit more wave attenuation (i.e., larger $1000/Q$) than the intact sample at a given tensile force, and the difference gradually becomes more significant as the tensile force increases (Fig. 7a). Similar trends of $1000/Q$ are observed for diabase specimens D-F-1 and D-F-3, but $1000/Q$ for D-F-2 is comparable to that for D-I throughout the tensile process (Fig. 7a). Wave attenuation ($1000/Q$) increases at a much higher rate for diabase specimens than for quartz diorite specimens with the tensile loading force (Fig. 7b & d). The value of $1000/Q$ for quartz diorite specimens ultimately increases by 560 %–730 %, while diabase specimens display the accumulated growth in $1000/Q$ of 2300 %–5700 % over the tensile process. The jointed quartz diorite specimens exhibit an increasing trend of $1000/Q$ similar to the intact sample (Fig. 7b). The accumulated increase in $1000/Q$ for the intact quartz diorite specimen is 1.1–1.3 times larger than that for jointed quartz diorite specimens. By comparison, the intact diabase specimen displays a much faster rate of the relative $1000/Q$ increase than the jointed diabase specimen (Fig. 7d). The $1000/Q$ growth for the intact diabase sample is 1.5–2.5 times higher than that for jointed diabase specimens.

Wave attenuation ($1000/Q$) exhibits approximately opposite altering trends to the dominant frequency (f_d) for rock specimens under tension (Figs. 6 and 7). Among all wave properties evaluated in this study, $1000/Q$ is the most sensitive to the uniaxial tensile loading, while A_{PTP} and S_{max} take second place.

3.2.5. Comparison of wave characteristics between intact and. Jointed rock samples

Stress-strain behavior and relative wave velocity change show consistent tend that D-F-3 is similar to its intact counterpart D-I (Figs. 3b

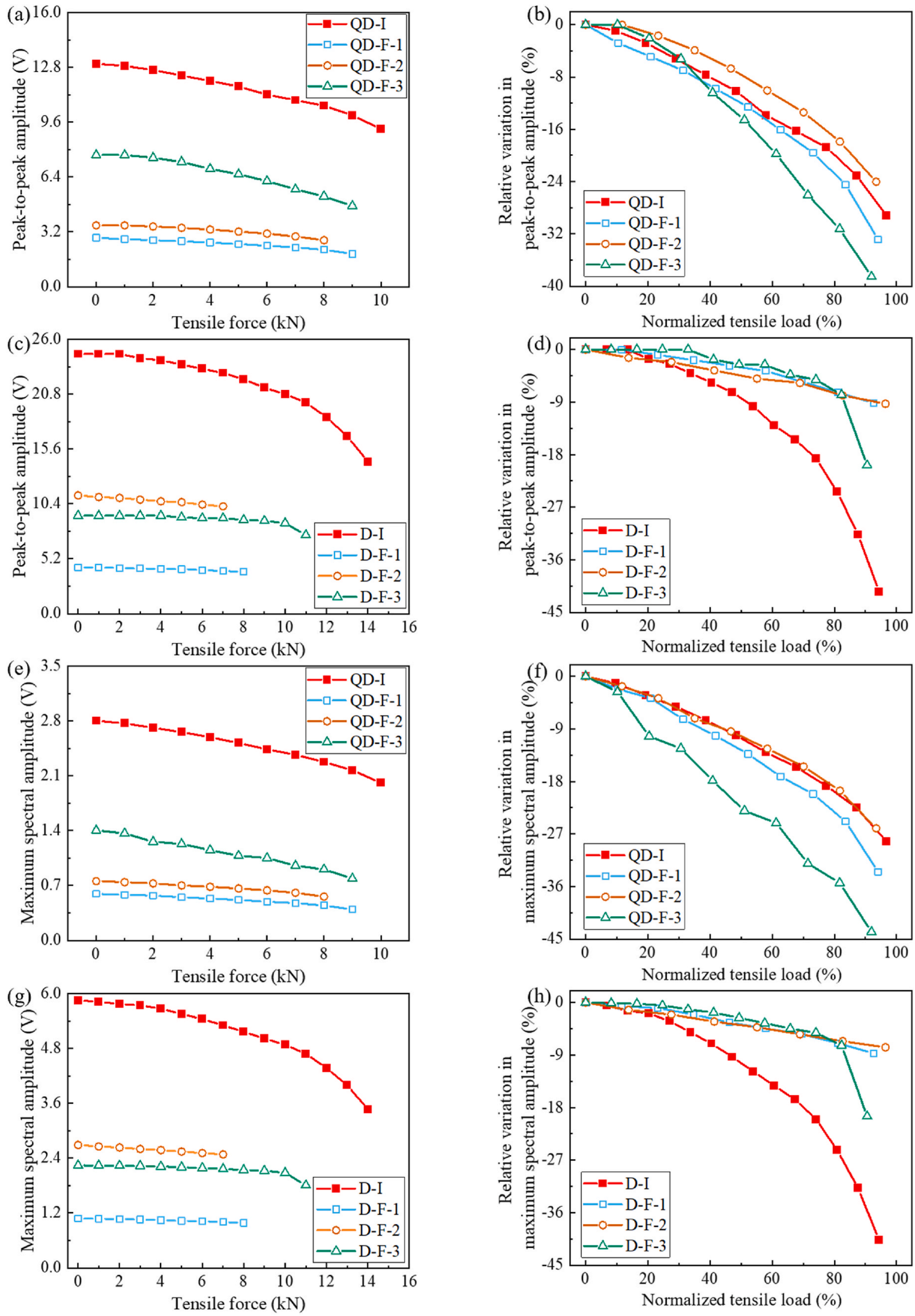

Fig. 5. Wave amplitudes and their relative variation during the tensile loading process for (a), (c), (e), and (g) Quartz diorite specimens, and (b), (d), (f), and (h) Diabase specimens. The normalized tensile load is determined by normalizing a specific tensile load to the ultimate load at the tensile failure.

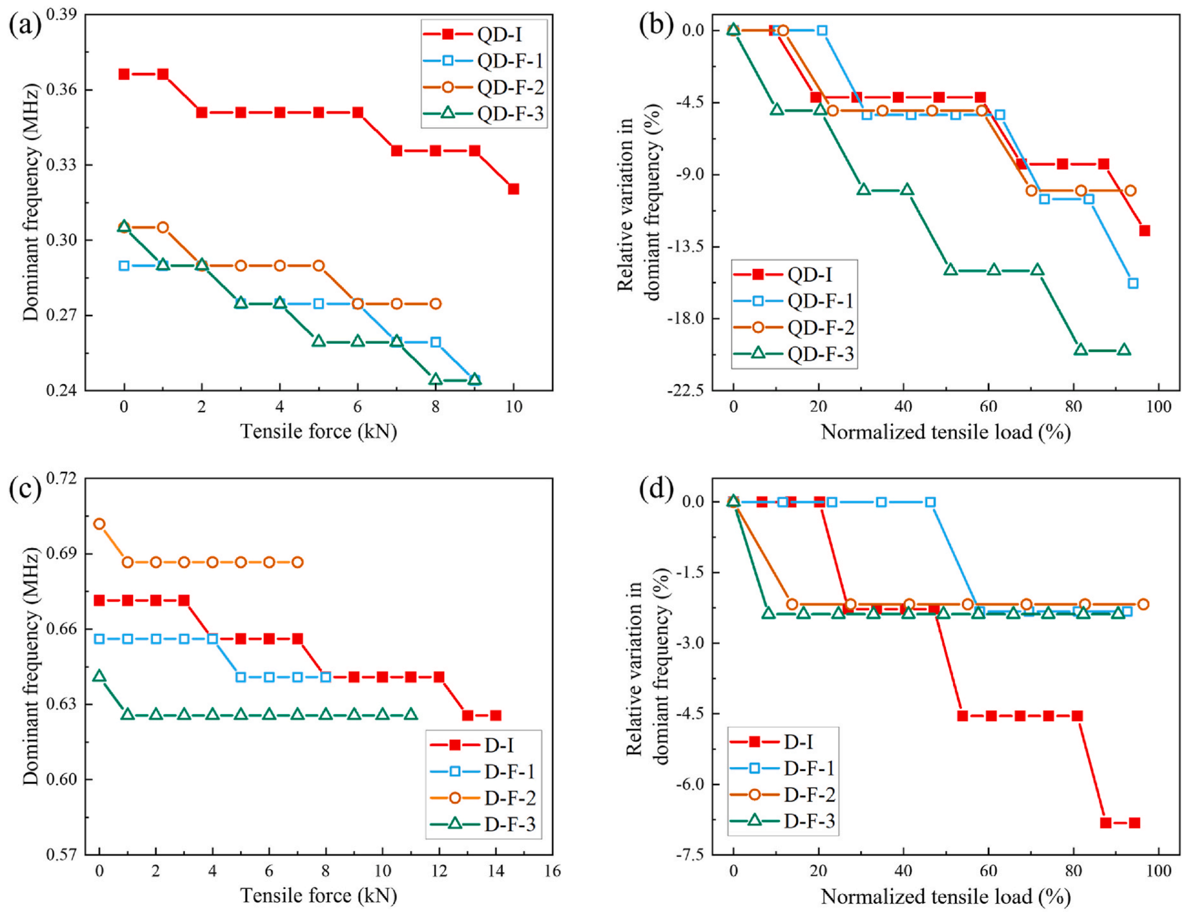

Fig. 6. Dominant frequency and corresponding relative variation during the tensile loading process for (a–b) Quartz diorite specimens and (c–d) Diabase specimens. The normalized tensile load is determined by normalizing a specific tensile load to the ultimate load at the tensile failure.

& 4d). However, relative changes in peak-to-peak amplitude (Fig. 5d), maximum spectral amplitude (Fig. 5h), dominant frequency (Fig. 6d), and wave attenuation (Fig. 7d) do not show such similarity between D-F-3 and D-I. Instead, jointed diabase samples show similar trends and are significantly different from the intact sample.

A significant drop was measured at the last data point in both peak-to-peak amplitude and maximum spectral amplitude in D-F-3 sample. Note that this is a significant drop in relative terms but not in absolute value. The absolute drop of this last data point is only a fraction (~5.8 %) of that in the last data point of the intact rock.

3.3. Static and dynamic fracture stiffness

Using the methods outlined in Section 2.5, we evaluate both the static and dynamic fracture stiffness of cemented rock fractures to better interpret the variations in elastic wave parameters under tensile stress. Specifically, dynamic fracture stiffness is assessed using transmitted wave data, while static fracture stiffness is determined from mechanical stress-displacement data. To facilitate the analysis of tension-induced variations, the fracture stiffness values are normalized to their corresponding pre-tension values, as shown in Fig. 8. This normalization allows for a more direct comparison of the effects of tensile loading on fracture stiffness.

For jointed quartz diorite specimens, the normalized static and dynamic fracture stiffness gradually and continuously decreases with the increasing tensile load (Fig. 8a). The maximum reduction in the normalized static fracture stiffness is 37.3 %–97.6 %, which is greater than that in the normalized dynamic fracture stiffness having a value of 33.1 %–64.4 %. Notably, sample QD-F-3, which is most similar to the intact specimen in terms of mechanical behavior and wave attributes, experienced the least reduction in static fracture stiffness, suggesting that the microcracking damage in the host rock of QD-F-3 is similar to that undertaken by the intact sample under tension. For jointed diabase specimens, the static fracture stiffness remains almost constant, whereas the dynamic fracture stiffness decreases by 7.1 %–13.3 % throughout the tensile process until the failure of the fractured diabase specimen (Fig. 8b).

3.4. Microstructural characterization

The microscopic images of the representative thin sections of epoxied post-mortem cemented rock fractures are illustrated in Fig. 9. The quartz diorite contains mineral grains, siliceous cementation, and heterogeneous distributed micro-cracks (Fig. 9a). For the cemented fracture embedded in the quartz diorite, the tension-induced crack propagates through the host rock, the cement, and the rock-cement interface, with several clearly identified deflections (Fig. 9b). The diabase consists mainly of the finer-grained matrix and uniformly dispersed micro-pores (Fig. 9b). The tension-driven failure occurs at the cement-diabase interface for the cemented fracture implanted in the diabase (Fig. 9b).

We conducted imaging analysis on twenty microscopic photos of thin sections with ImageJ. Fig. 10a illustrates the identification of microstructural features in some typical images. The quantitative size distribution of grains and micro defects in quartz diorite and diabase are presented in Fig. 10b and c. The diabase exhibits a narrower grain and microdefect size distribution than the quartz diorite. Fig. 10b shows that the grain size for the quartz diorite, mostly ranging from 0.211 mm to

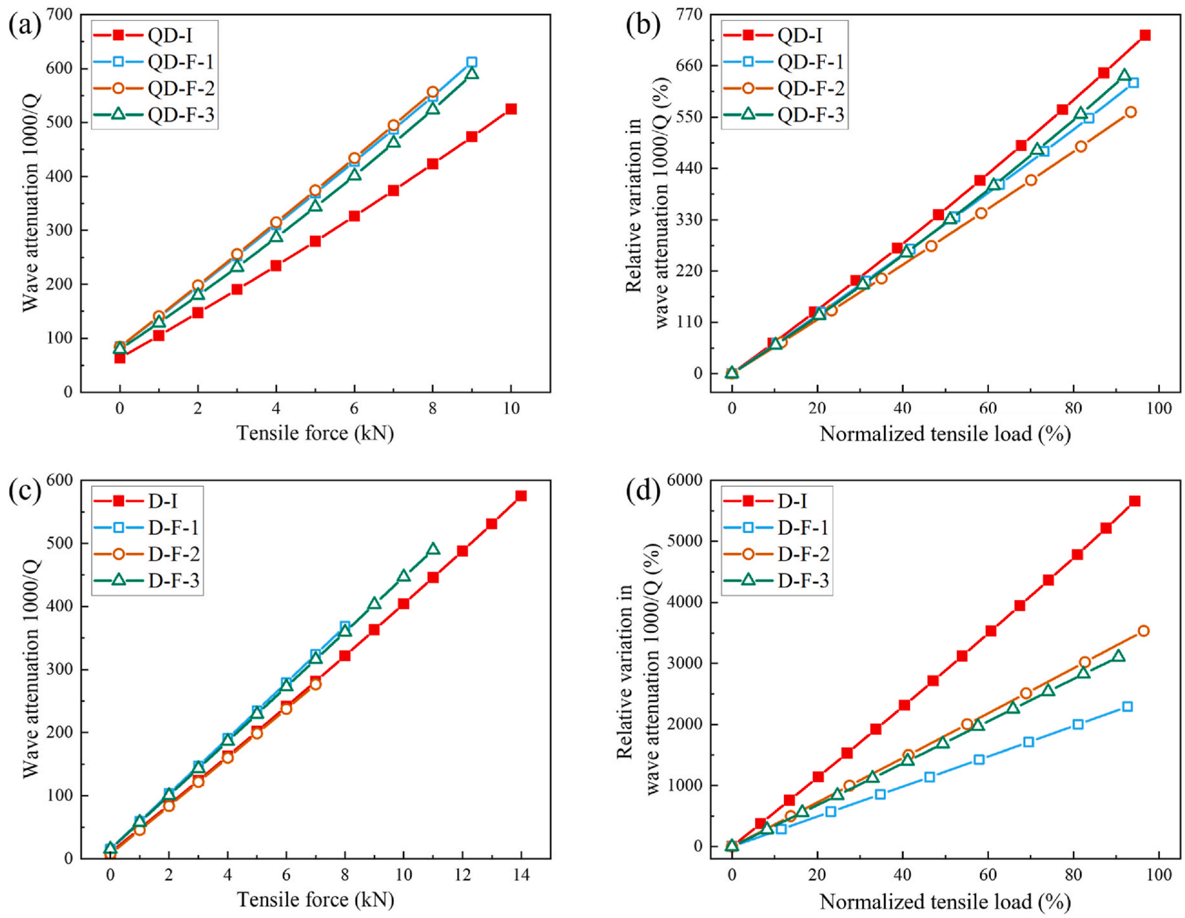

Fig. 7. Wave attenuation and its relative variation during the tensile loading process for (a–b) Quartz diorite specimens and (c–d) Diabase specimens. The normalized tensile load is determined by normalizing a specific tensile load to the ultimate load at the tensile failure.

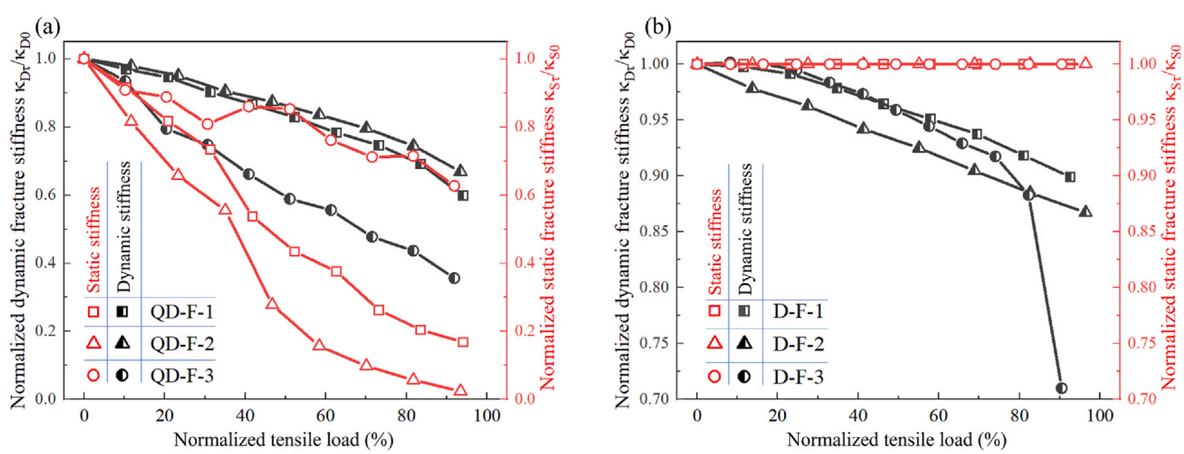

Fig. 8. The normalized dynamic and static fracture stiffness for (a) Quartz diorite and (b) Diabase fractured specimens throughout the tensile process. The normalized tensile load is determined by normalizing a specific tensile load to the ultimate load at the tensile failure.

0.589 mm, is much larger than that for the diabase, primarily within 0.024–0.199 mm. The micro defect size for the quartz diorite, mainly in the range of 0.106–0.298 mm, is greater than that for the diabase, mainly within the range of 0.039–0.148 mm (Fig. 10c).

4. Discussion

4.1. Comparison of elastic wave propagation under tension and compression

Our experiments show that tensile loading significantly impacts elastic wave propagation across cemented rock fractures, reducing wave velocity, amplitude, and dominant frequency while increasing attenuation. We make a comparison between our work and previous research

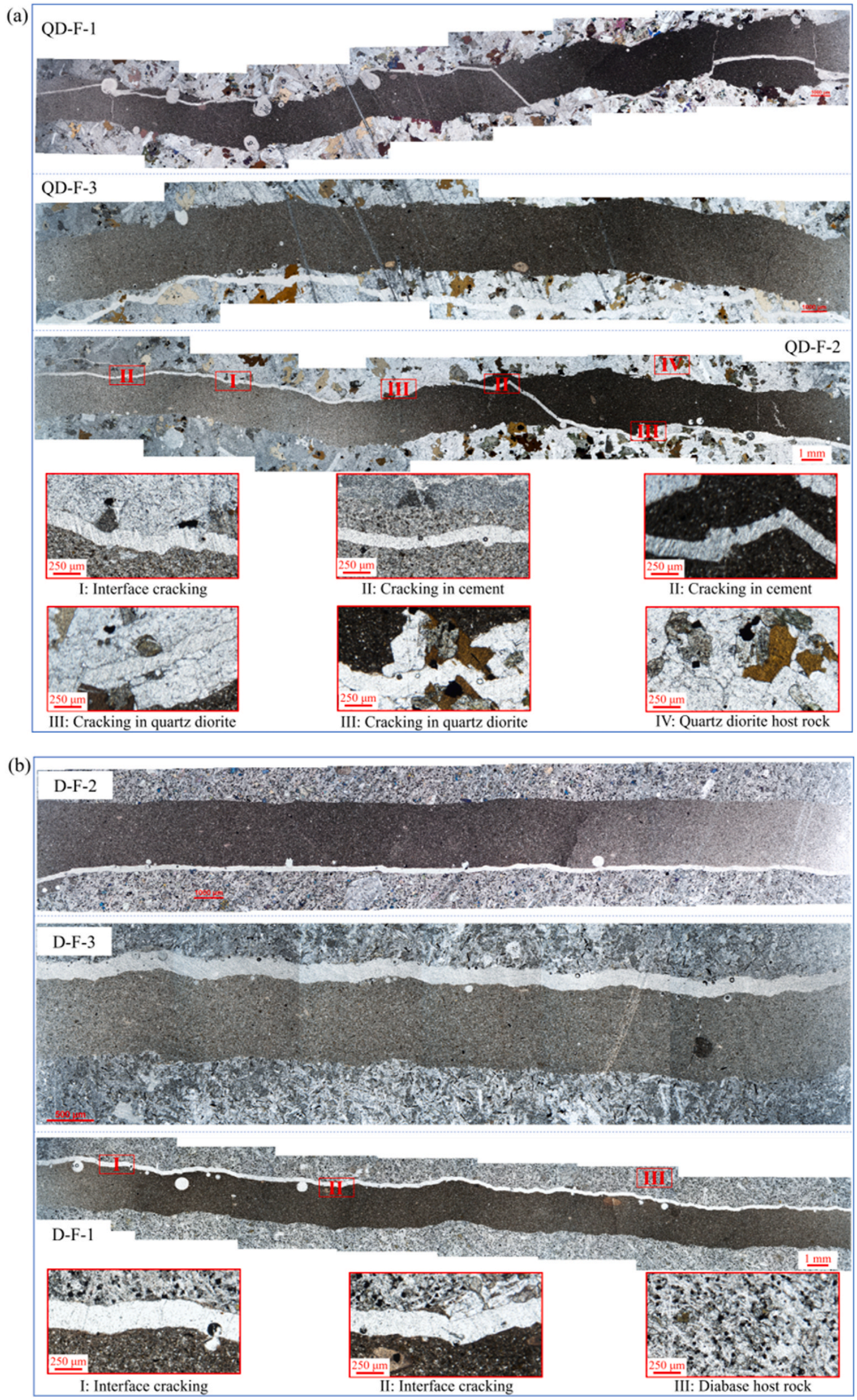

Fig. 9. Representative thin-section microphotographs of post-mortem cemented fractures in (a) Quartz diorite specimens and (b) Diabase specimens subjected to uniaxial tensile loading.

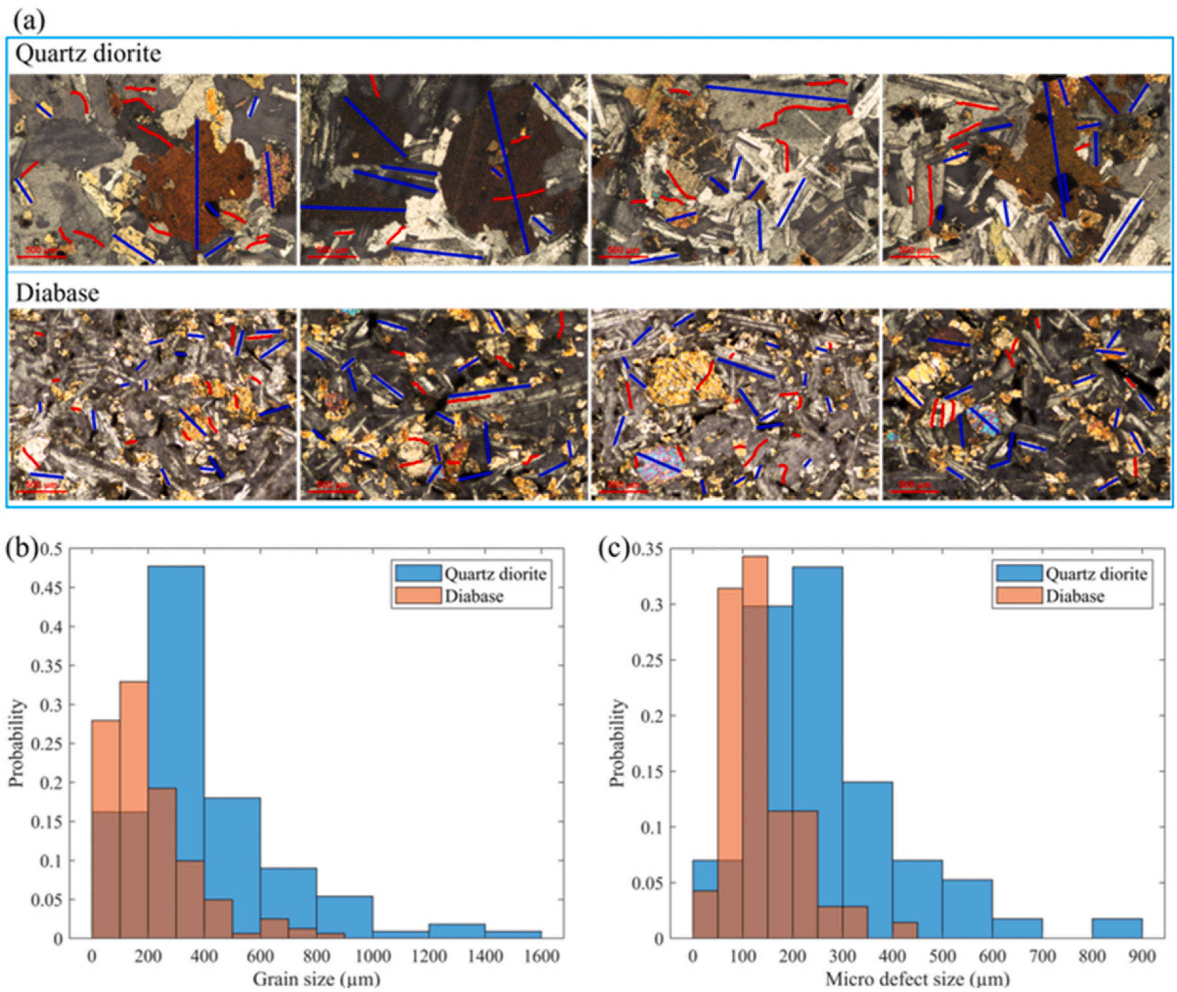

Fig. 10. (a). Illustration of evaluating microstructural features of rock samples based on microscopic photos of representative thin sections, where blue lines represent the long axis of grains, and red curves stands for micro defects; histograms showing the distribution of (b) grain size and (c) micro defect size for quartz diorite and diabase. (For interpretation of the references to colour in this figure legend, the reader is referred to the Web version of this article.)

focusing on wave propagation under compression loading,[10,17,50,51] where the stress for compression is set to be positive while that for tension is negative (Fig. 11). It indicates consistent trends in elastic wave behavior under both compression and tension stress conditions. The stress dependency of elastic wave properties can be attributed to the variation in stiffness of microscopic scale fractures. Under compression, increasing stress enhances fracture stiffness by closing apertures and increasing asperity contact.[52] In contrast, tensile stress promotes fracture opening through microcrack growth, which reduces fracture stiffness. The comparison also reveals that attenuation is more sensitive to tensile stress, whereas spectral amplitude is more responsive under compression. This suggests the potential of using different elastic wave parameters to distinguish between stress states in jointed rocks.

The variation in elastic wave properties can be linked to the elastic nonlinearity of the rock specimens,[53] arising from microcracks, grain-grain contacts, inter-grain cementation, etc.[41] The greater relative changes in wave properties observed in intact diabase than jointed ones indicate higher elastic nonlinearity in intact diabase. This observation is consistent with the findings of Manogharan et al.,[20,54] which attribute the reduced nonlinearity in jointed samples to strain localization near the fracture. The tension-driven debonding or weakening is observed at the cement-diabase interface, indicating that stress concentration occurs (Fig. 9). Conversely, jointed quartz diorite specimens exhibit greater nonlinearity than intact ones under tensile loading, which is likely due to the higher local compliance introduced by fractures in the host rock.[21,55] The stress-strain curves of quartz diorite (Fig. 3a) support this explanation, and further analysis reveals that the tension-driven cracks cross the host rock, host-cement interfaces, and cement, indicating significant strain in the host rock (Fig. 9). Our results suggest that microcracks in the host rock significantly influence wave propagation behavior, highlighting the need to consider both host rock and fracture properties when interpreting wave propagation behavior in surveying applications.

4.2. Influence of cemented rock fractures

Our results show that the tension-induced debonding for quartz diorite specimens with cemented fractures passes through the host rock, the cement, and the rock-cement interface, with multiple deflections observed (Fig. 9a). This behavior, consistent with the numerical results of Virgo et al.,[56] is likely due to the high strength contrast between the host rock and the cement and the kinking of the interfacial crack. The elastic moduli mismatch of the mineral phases creates stress concentrations, promoting crack initiation inside the quartz diorite under tension. The tightly interlocked crystals in quartz diorite also contribute to both intergranular and intragranular cracking, leading to significant microcracking in the host rock matrix during loading. In contrast, jointed diabase specimens fail mainly along the cement-diabase interface (Fig. 9b). It can be attributed to the weaker bond strength compared to the host rock, which concentrates tensile stress and directs tensile

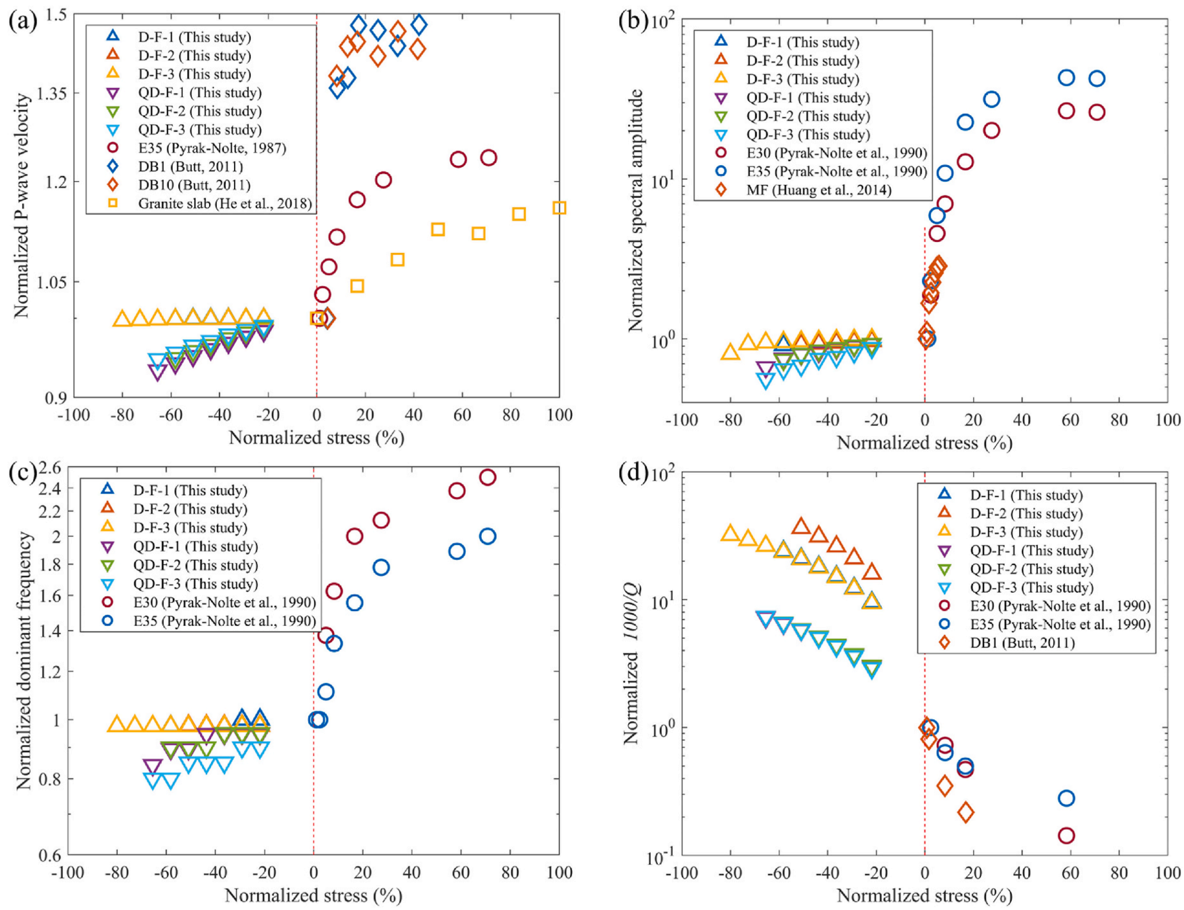

Fig. 11. Comparison of elastic wave behaviors across single rock fractures under uniaxial tension and compression: (a) normalized wave velocity, (b) normalized maximum spectral amplitude, (c) normalized dominant frequency, and (d) normalized value of 1000/Q. Note the vertical axes are at log scale for better visualization. Note that stresses extracted from those studies range from −7 MPa to 120 MPa; hence, we normalize compressive and tensile stresses by 120 MPa and −7 MPa, respectively. Besides, wave properties are normalized by the value at the start point of the loading.

fracture propagation.[57,58] Similar behavior has been observed in calcite-cemented fractures in field,[59] where the interface plays a critical role in controlling fracture propagation.

The mechanical response of jointed rocks with cemented fractures to tensile stress could be closely linked to their microstructural features.[60–65] Quartz diorite exhibits nonlinear stress-strain behavior similar to that of naturally fractured rocks with high density of pre-existing microcracks.[66] These microcracks intensify local stress concentrations and accelerate crack propagation,[67] forming multiple fracture process zones,[68,69] and reducing effective modulus under tensile load,[70] explaining the pronounced nonlinearity observed in the stress-strain curve. The diabase, on the other hand, shows a linear stress-strain relationship similar to limestone with natural fractures.[66] This is because the diabase has fewer pre-existing microcracks (Fig. 10), leading to a more uniform stress distribution in the host rock and crack propagation occurring primarily on the cemented joint interface and near the peak tensile load.[68]

The influence of cemented fractures on elastic wave behavior is similarly tied to microstructural changes. In quartz diorite, tensile stress expands pre-existing microcracks and pores, reducing elastic moduli, wave velocities, and amplitudes, while increasing attenuation. The largest pre-existing microcracks in quartz diorite, approximately 0.8 mm in size, can grow to the millimeter-to-centimeter scale that is comparable to the wavelength, causing substantial wave scattering. In contrast, diabase, with fewer microcracks, experiences less deformation and moderate changes in wave properties. However, the failure is rapid when the jointed sample reaches failure stress. The variation of wave attributes adjacent to failure can hardly be captured because the ultrasonic wave tests were conducted in incremental internal of 1 kN. The abrupt variations in peak-to-peak amplitude and maximum spectral amplitude for the D-F-3 specimen (Fig. 5d & h) may be a data point captured during the unstable cracking process right before the sample failure, which was not attained for D-F-1 and D-F-2. Future research using time-lapse wave measurements with higher time resolution could provide better insights.

4.3. Insights from static and dynamic fracture stiffness

Increases in wave velocity, wave amplitudes, dominant frequency, and a decrease in wave attenuation across individual rock fractures with increasing compressional load have been explained by the enhancement of fracture stiffness.[1,71] Static and dynamic fracture stiffness showed similar variation trends in the Quartz diorite specimens, but drastically different trends in the jointed diabase specimens. Static fracture stiffness was unchanged during the tensile loading process, while the dynamic fracture stiffness decreased by 7.1–13.3 %. The plausible explanation is that the microscopic damage at low strains modifies elastic wave velocity and dissipation, manifesting itself as a decrease in the dynamic fracture stiffness, while such low strains are not sensible by the quasi-static stress-strain measurements using strain gauges, resulting in negligible changes in the static fracture stiffness. The gradual decrease in the dynamic fracture stiffness could be a manifestation of the stable crack growth along the cement-diabase interface, while the sudden reduction in the dynamic fracture stiffness reflects the coalescence of cracks at the cement-diabase interface.

More significant decreases in the fracture stiffness are observed for jointed quartz diorite specimens rather than jointed diabase specimens with the increasing tensile load (Fig. 8). These observations are broadly consistent with the relative changes in elastic wave properties, particularly in the wave velocity and dominant frequency. It suggests that the microscopic characteristics of the host rocks dominate the tension-induced variation of fracture stiffness and then govern the elastic wave behaviors across cemented rock fractures. Dynamic fracture stiffness performs as a more reliable indicator of tensile deformation than static fracture stiffness because it reflects, consistently, the tensile loading process for both quartz diorite and diabase specimens, regardless of their differences in microstructural characteristics. In addition, dynamic fracture stiffness can be assessed using seismic waves, which is important for field applications.

5. Conclusions

In this study, we conducted ultrasonic pulse-transmission measurements and direct tensile tests on quartz diorite and diabase specimens, both with and without cemented fractures, to investigate elastic wave attributes across individual cemented rock fractures under tension. Results indicate that increasing tensile load decreases wave velocity, amplitude, and dominant frequency while increasing wave attenuation. Wave amplitude and attenuation are particularly sensitive to tensile loading.

Our measurements show that rock lithology significantly impacts elastic wave behavior under tension. Diabase samples exhibit higher wave velocity, greater amplitudes, higher frequency, and lower attenuation compared to quartz diorite specimens. Jointed diabase shows less change in wave attributes than intact diabase, indicating lower elastic nonlinearity. In contrast, jointed quartz diorite has more pronounced changes, suggesting higher elastic nonlinearity. The host rock type also influences fracture stiffness: jointed quartz diorite shows decreasing static and dynamic fracture stiffness, whereas jointed diabase exhibits reduced dynamic fracture stiffness but constant static fracture stiffness under tension. This difference is primarily attributed to the higher heterogeneity in quartz diorite, which promotes microcracking and stress redistribution more effectively than in diabase.

Our findings enhance the understanding of elastic wave responses and tensile mechanical properties of individual cemented rock fractures under uniaxial tension. Elastic wave changes can act as proxies for assessing deformation and damage in fractured rock masses subject to tensile loading, relevant to fluid injection, excavation, or seismic activity. However, quantifying the influence of rock matrix and cemented fractures remains challenging due to complex interactions among rock matrix properties, cement characteristics, and microstructural features. Advanced modeling and further experimental research are required for precise quantification. The focus on artificial fractures also calls for broader studies in diverse geological settings. Replicating in-situ stress conditions such as cyclic tension and mixed loading scenarios is essential for comprehensively understanding fracture behavior in both natural and engineered environments.

CRediT authorship contribution statement

Hui Yang: Writing – review & editing, Writing – original draft, Visualization, Validation, Methodology, Investigation, Formal analysis, Conceptualization. **Qi Zhao:** Writing – review & editing, Visualization, Supervision, Resources, Project administration, Investigation, Funding acquisition, Formal analysis, Data curation, Conceptualization. **Dongya Han:** Validation, Supervision, Methodology, Investigation, Conceptualization. **Qinghua Lei:** Writing – review & editing, Supervision, Resources, Project administration, Funding acquisition. **Huanyu Wu:** Visualization, Software, Methodology, Investigation. **Xiaolin Huang:** Writing – review & editing, Validation, Supervision, Investigation. **Zhiyi Chen:** Writing – review & editing, Supervision, Resources, Project administration, Funding acquisition. **Yu Huang:** Writing – review & editing, Supervision, Resources, Project administration, Funding acquisition.

Declaration of competing interest

The authors declare that they have no known competing financial interests or personal relationships that could have appeared to influence the work reported in this paper.

Acknowledgments

We sincerely thank Prof. J.G. Teng and Dr. Y. Xiang for providing the laboratory data on the ultra-high-performance cement used in this study. Dr. H. Yang is supported by the Joint Postdoc Scheme with Non-local Institutions by PolyU (P0042945). Dr. Q. Zhao is supported by the Early Career Scheme and the General Research Fund of the Research Grants Council of the Hong Kong SAR, China (Project No. PolyU 25220021, PolyU 15227222, and PolyU 15229723). Dr. D.Y. Han is supported by the National Natural Science Foundation of China (Grant No. 52204118). Dr. Q. Lei is grateful for the support from the Swiss National Science Foundation (Grant No. 189882) and the National Natural Science Foundation of China (Grant No. 41961134032).

Data availability

Data will be made available on request.

References

1. Pyrak-Nolte LJ. The seismic response of fractures and the interrelations among fracture properties. *Int J Rock Mech Min Sci Geomech Abstracts*. 1996;33(8):787–802. https://doi.org/10.1016/S0148-9062(96)00022-8.
2. Pyrak-Nolte LJ, Roy S. Monitoring fracture evolution with compressional-mode interface waves. *Geophys Res Lett*. 2000;27(20):3397–3400. https://doi.org/10.1029/1999GL011125.
3. Barton N. *Rock Quality, Seismic Velocity, Attenuation and Anisotropy*. first ed. CRC press; 2006.
4. Shreedharan S, Rivière J, Bhattacharya P, Marone C. Frictional state evolution during normal stress perturbations probed with ultrasonic waves. *J Geophys Res Solid Earth*. 2019;124(6):5469–5491. https://doi.org/10.1029/2018JB016885.
5. Winkler K, Nur A, Gladwin M. Friction and seismic attenuation in rocks. *Nature*. 1979;277(5697):528–531. https://doi.org/10.1038/277528a0.
6. Brenguier F, Campillo M, Hadziioannou C, Shapiro NM, Nadeau RM, Larose É. Postseismic relaxation along the San Andreas fault at Parkfield from continuous seismological observations. *science*. 2008;321(5895):1478–1481. https://doi.org/10.1126/science.1160.
7. Kaproth BM, Marone C. Slow earthquakes, preseismic velocity changes, and the origin of slow frictional stick-slip. *Science*. 2013;341(6151):1229–1232. https://doi.org/10.1126/science.1239577.
8. Scuderi MM, Marone C, Tinti E, Di Stefano G, Collettini C. Precursory changes in seismic velocity for the spectrum of earthquake failure modes. *Nat Geosci*. 2016;9(9):695–700. https://doi.org/10.1038/ngeo2775.
9. He TM, Zhao Q, Ha J, Xia K, Grasselli G. Understanding progressive rock failure and associated seismicity using ultrasonic tomography and numerical simulation. *Tunn Undergr Space Technol*. 2018;81:26–34. https://doi.org/10.1016/j.tust.2018.06.022.
10. Pyrak-Nolte LJ, Myer LR, Cook NG. Transmission of seismic waves across single natural fractures. *J Geophys Res Solid Earth*. 1990;95(B6):8617–8638. https://doi.org/10.1029/JB095iB06p08617.
11. Chen WY, Lovell CW, Haley GM, Pyrak-Nolte LJ. Variation of shear-wave amplitude during frictional sliding. *Int J Rock Mech Min Sci Geomech Abstracts*. 1993;30(7):779–784. https://doi.org/10.1016/0148-9062(93)90022-6.
12. Fratta D, Santamarina J. Shear wave propagation in jointed rock: state of stress. *Geotechnique*. 2002;52(7):495–505. https://doi.org/10.1680/geot.2002.52.7.495.
13. Zhao J, Cai JG, Zhao XB, Li HB. Experimental study of ultrasonic wave attenuation across parallel fractures. *Geomech. Geoengin.* 2006;1(2):87–103. https://doi.org/10.1080/17486020600834613.
14. Lubbe R, Sothcott J, Worthington MH, McCann C. Laboratory estimates of normal and shear fracture compliance. *Geophys Prospect*. 2008;56(2):239–247. https://doi.org/10.1111/j.1365-2478.2007.00688.x.
15. Nagata K, Nakatani M, Yoshida S. Monitoring frictional strength with acoustic wave transmission. *Geophys Res Lett*. 2008;35(6). https://doi.org/10.1029/2007GL033146.
16. Hedayat A, Pyrak-Nolte LJ, Bobet A. Precursors to the shear failure of rock discontinuities. *Geophys Res Lett*. 2014;41(15):5467–5475. https://doi.org/10.1002/2014GL060848.

17. Huang X, Qi S, Guo S, Dong W. Experimental study of ultrasonic waves propagating through a rock mass with a single joint and multiple parallel joints. *Rock Mech Rock Eng*. 2014;47:549–559. https://doi.org/10.1007/s00603-013-0399-2.
18. Hedayat A, Haeri H, Hinton J, Masoumi H, Spagnoli G. Geophysical signatures of shear-induced damage and frictional processes on rock joints. *J Geophys Res Solid Earth*. 2018;123(2):1143–1160. https://doi.org/10.1002/2017JB014773.
19. Nakagawa S, Nihei KT, Myer LR. Shear-induced conversion of seismic waves across single fractures. *Int J Rock Mech Min Sci*. 2000;37(1-2):203–218. https://doi.org/10.1016/S1365-1609(99)00101-X.
20. Manogharan P, Wood C, Rivière J, Elsworth D, Marone C, Shokouhi P. Elastodynamic nonlinear response of dry intact, fractured and saturated rock. In: *ARMA US Rock Mechanics/Geomechanics Symposium 2020, Jun 28*. ARMA; 2020.
21. Shokouhi P, Jin J, Wood C, et al. Dynamic stressing of naturally fractured rocks: on the relation between transient changes in permeability and elastic wave velocity. *Geophys Res Lett*. 2020;47(1), e2019GL083557. https://doi.org/10.1029/2019GL083557.
22. Wood CE, Shokouhi P, Manogharan P, Rivère J, Elsworth D, Marone C. Imaging elastodynamic and hydraulic properties of in situ fractured rock: an experimental investigation exploring effects of dynamic stressing and shearing. *J Geophys Res Solid Earth*. 2021;126(11), e2020JB021521. https://doi.org/10.1029/2020JB021521.
23. Fan LF, Wang LJ, Wang M, Wu ZJ. Investigation of stress wave transmission across a nonlinearly jointed complex rock mass. *Int J Rock Mech Min Sci*. 2020;136, 104485. https://doi.org/10.1016/j.ijrmms.2020.104485.
24. Zhang Y, Zhao GF, Wei X, Li H. A multifrequency ultrasonic approach to extracting static modulus and damage characteristics of rock. *Int J Rock Mech Min Sci*. 2021; 148, 104925. https://doi.org/10.1016/j.ijrmms.2021.104925.
25. Ramsay JG. The crack–seal mechanism of rock deformation. *Nature*. 1980;284 (5752):135–139. https://doi.org/10.1038/284135a0.
26. Laubach SE. Practical approaches to identifying sealed and open fractures. *AAPG (Am Assoc Pet Geol) Bull*. 2003;87(4):561–579. https://doi.org/10.1306/11060201106.
27. Lander RH, Laubach SE. Insights into rates of fracture growth and sealing from a model for quartz cementation in fractured sandstones. *GSA Bulletin*. 2015;127(3-4): 516–538. https://doi.org/10.1130/B31092.1.
28. Caputo R. Why joints are more abundant than faults. A conceptual model to estimate their ratio in layered carbonate rocks. *J Struct Geol*. 2010;32(9):1257–1270. https://doi.org/10.1016/j.jsg.2009.05.011.
29. Shang J, Hencher SR, West LJ. Tensile strength of geological discontinuities including incipient bedding, rock joints and mineral veins. *Rock Mech Rock Eng*. 2016;49:4213–4225. https://doi.org/10.1007/s00603-016-1041-x.
30. Han D, Zhu J, Leung YF. Deformation of healed rock joints under tension: experimental study and empirical model. *Rock Mech Rock Eng*. 2020;53:3353–3362. https://doi.org/10.1007/s00603-020-02103-5.
31. Bons PD, Elburg MA, Gomez-Rivas E. A review of the formation of tectonic veins and their microstructures. *J Struct Geol*. 2012;43:33–62. https://doi.org/10.1016/j.jsg.2012.07.005.
32. Ramsey JM, Chester FM. Hybrid fracture and the transition from extension fracture to shear fracture. *Nature*. 2004;428(6978):63–66. https://doi.org/10.1038/nature02333.
33. Silberschmidt V, Silberschmidt V. Analysis of cracking in rock salt. *Rock Mech Rock Eng*. 2000;33(1):53–70. https://doi.org/10.1007/s006030050004.
34. Han D, Yang H. Effects of tensile stresses on wave propagation across stylolitic rock joints. *Int J Rock Mech Min Sci*. 2021;139, 104617. https://doi.org/10.1016/j.ijrmms.2021.104617.
35. Teng JG, Xiang Y, Yu T, Fang Z. Development and mechanical behaviour of ultra-high-performance seawater sea-sand concrete. *Adv Struct Eng*. 2019;22(14): 3100–3120. https://doi.org/10.1177/1369433219858.
36. D-3976. Standard test method for splitting tensile strength of intact rock core specimens. In: *American Society for Testing Material*. ASTM Int.; 1986.
37. Eshbach OW, Tapley BD. *Eshbach's Handbook of Engineering Fundamentals*. fourth ed. John Wiley & Sons; 1990.
38. Yang H, Duan H, Zhu J. Thermal effect on compressional wave propagation across fluid-filled rock joints. *Rock Mech Rock Eng*. 2021;54(1):455–462. https://doi.org/10.1007/s00603-020-02254-5.
39. Yang H, Duan HF, Zhu J. Effects of filling fluid type and composition and joint orientation on acoustic wave propagation across individual fluid-filled rock joints. *Int J Rock Mech Min Sci*. 2020;128, 104248. https://doi.org/10.1016/j.ijrmms.2020.104248.
40. Yang H, Duan HF, Zhu J. Experimental study on the role of clay mineral and water saturation in ultrasonic P-wave behaviours across individual filled rock joints. *Int J Rock Mech Min Sci*. 2023;168, 105393. https://doi.org/10.1016/j.ijrmms.2023.105393.
41. Renaud G, Le Bas PY, Johnson PA. Revealing highly complex elastic nonlinear (anelastic) behavior of Earth materials applying a new probe: dynamic acoustoelastic testing. *J Geophys Res Solid Earth*. 2012;117(B6):1–7. https://doi.org/10.1029/2011JB009127.
42. Renaud G, Talmant M, Callé S, Defontaine M, Laugier P. Nonlinear elastodynamics in micro-inhomogeneous solids observed by head-wave based dynamic acoustoelastic testing. *J Acoust Soc Am*. 2011;130(6):3583–3589. https://doi.org/10.1121/1.3652871.
43. King MS. Wave velocities in rocks as a function of changes in overburden pressure and pore fluid saturants. *Geophysics*. 1966;31(1):50–73. https://doi.org/10.1190/1.1439763.
44. Molyneux JB, Schmitt DR. First-break timing: Arrival onset times by direct correlation. Geophysics. 199; 64(5): 1492-1501. https://doi.org/10.1190/1.1444653.
45. Brillouin L. *Wave Propagation and Group Velocity*. Academic press; 2013.
46. Molyneux JB, Schmitt DR. Compressional-wave velocities in attenuating media: a laboratory physical model study. *Geophysics*. 2000;65(4):1162–1167. https://doi.org/10.1190/1.1444809.
47. Toksöz M, Johnston DH, Timur A. Attenuation of seismic waves in dry and saturated rocks: I. Laboratory measurements. *Geophysics*. 1979;44(4):681–690. https://doi.org/10.1190/1.1440969.
48. Bandis SC, Lumsden AC, Barton NR. Fundamentals of rock joint deformation. *Int J Rock Mech Min Sci Geomech Abstracts*. 1983;20(6):249–268. https://doi.org/10.1016/0148-9062(83)90595-8.
49. Pyrak-Nolte LJ, Nolte DD. Frequency dependence of fracture stiffness. *Geophys Res Lett*. 1992;19(3):325–328. https://doi.org/10.1029/91GL03179.
50. Pyrak LJ. *Seismic Visibility of Fractures*. Berkeley: University of California; 1988.
51. Butt SD. Experimental measurement of P-wave attenuation due to fractures over the 100 to 300 kHz bandwidth. *Pure Appl Geophys*. 2001;158:1783–1796. https://doi.org/10.1007/PL00001243.
52. Hopkins D, Cook N, Myer L. Normal joint stiffness as a function of spatial geometry and surface roughness. In: *Paper Presented at the International Symposium on Rock Joints Held at Loen*. 1990:203–210.
53. Rivière J, Pimienta L, Scuderi M, et al. Frequency, pressure, and strain dependence of nonlinear elasticity in Berea Sandstone. *Geophys Res Lett*. 2016;43(7):3226–3236. https://doi.org/10.1002/2016GL068061.
54. Manogharan P, Wood C, Marone C, Elsworth D, Rivière J, Shokouhi P. Nonlinear elastodynamic behavior of intact and fractured rock under in-situ stress and saturation conditions. *J Mech Phys Solid*. 2021;153, 104491. https://doi.org/10.1016/j.jmps.2021.104491.
55. Jin J, Rivière J, Ohara Y, Shokouhi P. Dynamic acousto-elastic response of single fatigue cracks with different microstructural features: an experimental investigation. *J Appl Phys*. 2018;124(7), 075303. https://doi.org/10.1063/1.5036531.
56. Virgo S, Abe S, Urai JL. Extension fracture propagation in rocks with veins: Insight into the crack-seal process using Discrete Element Method modeling. J Geophys Res Solid Earth 201; 118(10): 5236-5251. https://doi.org/10.1002/2013JB010540.
57. Akisanya AR, Fleck NA. Analysis of a wavy crack in sandwich specimens. *Int J Fract*. 1992;55(1):29–45. https://doi.org/10.1007/BF00018031.
58. Akisanya AR, Fleck NA. Brittle fracture of adhesive joints. *Int J Fract*. 1992;58(2): 93–114. https://doi.org/10.1007/BF00019971.
59. Tabatabaei M, Taleghani AD, Hooker J. Debonding of cemented natural fractures during core recovery. *J Struct Geol*. 2021;144, 104272. https://doi.org/10.1016/j.jsg.2020.104272.
60. Mahabadi OK, Tatone BS, Grasselli G. Influence of microscale heterogeneity and microstructure on the tensile behavior of crystalline rocks. *J Geophys Res Solid Earth*. 2014;119(7):5324–5341. https://doi.org/10.1002/2014JB011064.
61. Ma X, Zoback MD. Laboratory experiments simulating poroelastic stress changes associated with depletion and injection in low-porosity sedimentary rocks. *J Geophys Res Solid Earth*. 2017;122(4):2478–2503. https://doi.org/10.1002/2016JB013668.
62. Potyondy DO, Cundall P. A bonded-particle model for rock. *Int J Rock Mech Min Sci*. 2004;41(8):1329–1364. https://doi.org/10.1016/j.ijrmms.2004.09.011.
63. Griffith AA. The phenomena of rupture and flow in solids. *Series A, Containing Papers of A Mathematical or Physical Character*. 1921;221(582-593):163–198. https://doi.org/10.1098/rsta.1921.0006.
64. Hashiba K, Fukui K. Effect of water on the deformation and failure of rock in uniaxial tension. *Rock Mech Rock Eng*. 2015;48(5):1751–1761. https://doi.org/10.1007/s00603-014-0674-x.
65. Bruno G, Kachanov M, Sevostianov I, Shyam A. Micromechanical modeling of non-linear stress-strain behavior of polycrystalline microcracked materials under tension. *Acta Mater*. 2019;164:50–59. https://doi.org/10.1016/j.actamat.2018.10.024.
66. Cen D, Huang D, Song Y, Jiang Q. Direct tensile behavior of limestone and sandstone with bedding planes at different strain rates. *Rock Mech Rock Eng*. 2020;53(6): 2643–2651. https://doi.org/10.1007/s00603-020-02070-x.
67. Blair S, Cook N. Analysis of compressive fracture in rock using statistical techniques: Part I. A non-linear rule-based model. *Int J Rock Mech Min Sci*. 1998;35(7):837–848. https://doi.org/10.1016/S0148-9062(98)00008-4.
68. Hoagland RG, Hahn GT, Rosenfield AR. Influence of microstructure on fracture propagation in rock. *Rock Mech*. 1973;5(2):77–106. https://doi.org/10.1007/BF01240160.
69. Ouchterlony F. Review of fracture toughness testing of rock. *SM Arch*. 1982;7: 131–211.
70. Atkinson BK. Subcritical crack growth in geological materials. *J Geophys Res Solid Earth*. 1984;89(B6):4077–4114. https://doi.org/10.1029/JB089iB06p04077.
71. Zhu J, Perino A, Zhao G, et al. Seismic response of a single and a set of filled joints of viscoelastic deformational behaviour. *Geophys J Int*. 2011;186(3):1315–1330. https://doi.org/10.1111/j.1365-246X.2011.05110.x.